

## 4D-Var data assimilation in a nested, coastal ocean model: A Hawaiian case study

I. Janeković,<sup>1,2</sup> B. S. Powell,<sup>1</sup> D. Matthews,<sup>1</sup> M. A. McManus,<sup>1</sup> and J. Sevadjian<sup>1</sup>

Received 24 May 2013; revised 2 September 2013; accepted 4 September 2013.

[1] State estimation techniques have been well established in open ocean systems; however they are less often used in coastal applications due to nonlinearity. Using 4D-variational data assimilation in a triple one-way nested system, we investigate the processes that control coastal dynamics for a test case along the western coast of Oahu, Hawaii. All available observations are combined with the model dynamics for 13 months. Over this time, the residual error between the model and observations was improved by nearly 30% in the surface temperature and 34% in the alongshore ADCP currents. The barotropic and baroclinic tides are found dominate the local circulation; however, island and atmospheric interaction generates an island wake effect that is important to the subtidal dynamics of the region. The baroclinic tides exhibit well-defined energy paths, and the initial condition corrections, despite altering the density waveguide, have little influence on the propagation of the baroclinic energy, which is controlled by the propagation of baroclinic tides generated outside of the domain. We find the larger-scale, advected dynamics control the local surface circulation through boundary condition adjustment, accounting for 45% of the total corrections made via data assimilation system. The initial conditions controls little of the evolution of this local, coastal flow and has a short persistence. The wind stress control vector is important in the central region of the domain inducing flow toward the lee of the island. Our results reveal that coastal studies may not be initial value problems, rather they are forced problems that require a knowledge of the large-scale energy propagated into the region.

**Citation:** Janeković, I., B. S. Powell, D. Matthews, M. A. McManus, and J. Sevadjian (2013), 4D-Var data assimilation in a nested, coastal ocean model: A Hawaiian case study, *J. Geophys. Res. Oceans*, 118, doi:10.1002/jgrc.20389.

### 1. Introduction

[2] Variational state estimation techniques have been well established in global and regional ocean modeling systems with spatial resolutions on the order of 1–100 km and temporal of a few days [Moore *et al.*, 2011a; Powell *et al.*, 2009; Broquet *et al.*, 2009; Matthews *et al.*, 2012] to decades [Köhl *et al.*, 2007; Stammer *et al.*, 2002, 2003, 2004]. Variational methods aim to minimize the residuals between observed data and the model trajectory over a given period of time through the adjustments of control parameters. To accomplish this, a cost function is minimized via conjugate gradient that measures: (i) the sum of the adjustments weighted by the model uncertainty in the initial conditions (ICs), boundary conditions (BCs), and forcing fields (FFs),

and (ii) the sum over time of all residuals between data and model at observation locations, weighted by the observational error covariances. To solve directly, the variational method relies on linear variational calculus that limits the spatial and temporal scales over which linearity is valid. This may significantly limit the application of variational methods in complex coastal regions that may be characterized by high spatial resolutions,  $O(100\text{ m})$ , and short temporal scales.

[3] The first data assimilation schemes used in the high-resolution limited area models have been constrained by empirical approaches, such as simple optimal interpolation methods [Demirov *et al.*, 2003]. Because high-resolution models can resolve strong nonlinear currents and fast moving circulation, the controllability of the nonlinear numerical models becomes the limiting factor [Köhl and Willebrand, 2002] for linear methods. This is particularly true when performing a high-resolution assimilation experiment for a longer assimilation period when perturbations can grow exponentially due to the lack of nonlinear processes in the linearized models [Zhu *et al.*, 2002]. To avoid this problem, previous experiments have employed a variety of methods, such as filtering the nonlinear model [Köhl and Willebrand, 2002] or significantly increasing diffusivity and viscosity in the linear model [Hoteit *et al.*, 2005].

<sup>1</sup>Department of Oceanography, Marine Sciences Building, Honolulu, Hawaii, USA.

<sup>2</sup>Center for Environmental and Marine Research, Institute Rudjer Bošković, Zagreb, Croatia.

Corresponding author: I. Janeković, Center for Environmental and Marine Research, Institute Rudjer Bošković, Bijenička c. 54, 10000 Zagreb, Croatia. (ivica@irb.hr)

These assumptions may become obstacles in reconstructing the ocean circulation and its variability in high-resolution models. A partial solution is to shorten assimilation time window where the linear assumption remains valid [Powell *et al.*, 2008]. In addition to the time window, high-resolution coastal systems are usually nested within an outer model, and special attention must be given to the boundary conditions adjustments to prevent assimilation increments from decoupling the nested model from the outer counterpart.

[4] The Hawaiian archipelago (Figure 1) is characterized by dynamics at a wide range of spatial and temporal scales. The islands are located in the deep basin of the northern Pacific and significantly influence the dynamics and climate features of the Pacific basin [Xie *et al.*, 2001]. Under influence of the trade winds, the islands alter the dynamics in the atmosphere [Xie *et al.*, 2001] and the oceanic feedback response. Along the Hawaiian island chain, Chavanne *et al.* [2002] used scatterometer observations of the wind to show that horizontal divergence and convergence in the surface flow must be compensated with vertical one reaching values of  $3 \text{ m day}^{-1}$ . Instantaneous values may be larger, affecting the depth of the thermocline as well as the intensity and energetics of eddies found in the lee of the islands. These sharp gradients in the wind fields of the lee of the islands are favorable for developing island wake dynamics [Wolanski *et al.*, 1996; Dong and McWilliams, 2007]. The

islands are steep oceanic mountains without extending shelves such that large-scale dynamics may affect the inner-shelf, and the slope helps maintain relative vorticity [Dong and McWilliams, 2007]. Such a region, where the steep slope descends over 2.5 km deep only 15 km away from the coast, can be found west of Oahu. In addition, to the northwest of Oahu is Kaena Ridge, a well-known internal tide generation site [Merrifield and Holloway, 2002; Nash *et al.*, 2006; Carter *et al.*, 2008; Chavanne *et al.*, 2010], characterized with strong barotropic and baroclinic dynamics and complex bathymetry. In addition, exchange between the mean island circulation currents occurs through this channel Lumpkin [1998] and Lumpkin and Flament [2013]. Barotropic  $M_2$  is the dominant tidal constituent and is nearly perpendicular to Kaena Ridge inducing strong barotropic to baroclinic tidal conversion. Tidally induced internal waves are a significant signal for the majority of Hawaiian island dynamics, with over 50% of the velocity energy originating in the internal tide spectrum. The western coast of Oahu lies in a region where all of these dynamical processes are equally present, and is dominated by surface and internal tide processes as described in McManus *et al.* [2008]. The region provides an ideal test bed for high-resolution numerical modeling and data assimilation techniques.

[5] In order to understand the processes that control the dynamics and particle advection along the western coast of Oahu, we utilize 1 year of high-resolution Acoustic Doppler Current Profiler (ADCP) data available along with satellite data and other in situ observations to constrain a high-resolution numerical model. This is used to examine the dynamical control of the region from the large-scale (influence on the boundary conditions), wind forcing (influence on the atmospheric forcing), and the density (influence on the initial conditions) in a nested model of this dynamic regime. In order to model the system correctly, one should know (i) what are the major control mechanisms responsible for dynamics and (ii) what increments from the data assimilation procedure provide the dynamical control. We used advanced 4D-Var data assimilation to combine the available time-dependent observations with the numerical model dynamics. Observations in the region are sparse, so we use all available observations from July 2009 through August 2010. These data include current magnitude and direction from the ADCPs, remote sensed satellite sea surface temperature (SST), and conductivity/temperature/depth (CTD) data in order to better constrain dynamics of the modeling system.

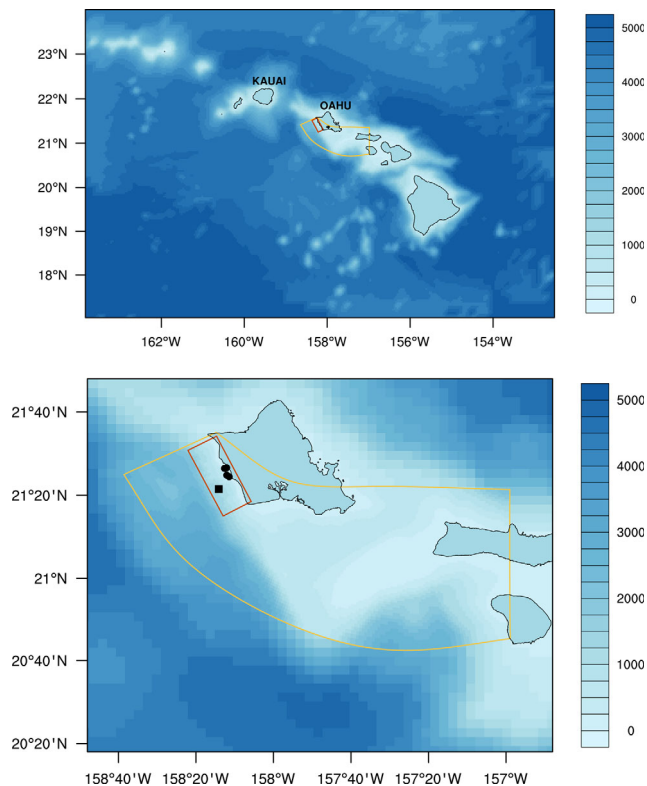


**Figure 1.** Hawaii model domains and bathymetry for nested models; outermost 4 km (top), intermediate 600–2500 m (yellow), and the finest 200–600 m grid (red). ADCP and Hawaii Ocean Time Series CTD locations used inside the finest grid and 4D-Var system are denoted as black dots and black square in the bottom figure.

## 2. Model, Data Assimilation, and Observations

### 2.1. Model

[6] The modeling component of our study is based on the Regional Ocean Modeling System (ROMS): a free-surface, hydrostatic, primitive equation model discretized with a terrain following vertical coordinate system [Shchepetkin and McWilliams, 2005]. Multiple subgrid scale parameterizations of vertical mixing and several options for open boundary conditions have been included. Time splitting of barotropic and baroclinic motions enables efficient integration. ROMS has been widely applied in many applications, from planetary scales down to estuarine environments. In

addition, ROMS offers a suite of state-of-the-art dynamical analysis tools, including adjoint, tangent-linear, and linear models for advanced variational data assimilation [Moore et al., 2011b, 2004; Powell et al., 2008, 2012] as well as a number of advanced biological models [Fennel et al., 2006; Fiechter et al., 2009].

## 2.2. Four-Dimensional Variational Formulation

[7] We utilize ocean state estimation based on the incremental, four-dimensional variational (4D-Var) formulation of Courtier et al. [1994] with the ROMS implementation described in detail by Moore et al. [2011b]. The two primary reasons for using the 4D-Var method in our system are (i) we can use observations at the exact observation times (crucial for tidal processes) with appropriate errors (not at the single time like in 3D-Var or optimal interpolation) and (ii) use the time-dependent dynamics of the model

to evolve the error covariance and constrain the system using the model physics rather than fixed statistics.

[8] We performed the state estimation over 4 day assimilation cycles to compute a control vector,  $\delta\mathbf{z}$ , composed of the increments to the initial conditions,  $\delta\mathbf{x}(0)$ , surface atmospheric forcing in time,  $\delta\mathbf{x}_f(t)$ , and the boundary conditions in time,  $\delta\mathbf{x}_\Omega(t)$ , such that  $\delta\mathbf{z} = (\delta\mathbf{x}(0), \delta\mathbf{x}_f(t), \delta\mathbf{x}_\Omega(t))$ . As described in Broquet et al. [2011], the quadratic cost function used in the minimization procedure is comprised of two components: the first,  $J_o$ , penalizes the residuals,  $\mathbf{d}$ , between the model and the observations,  $\mathbf{y}$ , as given by  $\mathbf{d} = \mathbf{y} - \mathcal{H}(\mathbf{x}(t))$ , where  $\mathbf{x}(t)$  is the model solution and  $\mathcal{H}$  samples the solution at the observation locations and times. The linear operator that maps the increments,  $\delta\mathbf{x}$  to the observation location and time is denoted as  $\mathbf{H}$ . The second part in the quadratic cost function is  $J_b$  that penalizes deviations from the *prior* model estimate defined as

$$J = \frac{1}{2} \underbrace{(\mathbf{G}\delta\mathbf{z} - \mathbf{d})^T \mathbf{R}^{-1} (\mathbf{G}\delta\mathbf{z} - \mathbf{d})}_{J_o} + \frac{1}{2} \underbrace{\left[ (\delta\mathbf{x}(0))^T \mathbf{P}_0^{-1} (\delta\mathbf{x}(0)) + (\delta\mathbf{x}_f(t))^T \mathbf{P}_f^{-1} (\delta\mathbf{x}_f(t)) + (\delta\mathbf{x}_\Omega(t))^T \mathbf{P}_\Omega^{-1} (\delta\mathbf{x}_\Omega(t)) \right]}_{J_b}, \quad (1)$$

where  $\mathbf{G}$  is the integration of the tangent-linear model (TLM) sampled at the observational space-time locations,  $\mathbf{G}^T$  is the adjoint of  $\mathbf{G}$ ,  $\mathbf{R}$  is the representational covariance error of the observations, and  $\mathbf{P}_0$ ,  $\mathbf{P}_f$ ,  $\mathbf{P}_\Omega$  are the background covariance matrices for the ICs, FFs, and BCs, respectively. As covariance terms are not known a priori, we utilize a factorization technique [Weaver and Courtier, 2001] by evaluating Gaussian diffusion of the variance over previously specified decorrelation error length scales. Based on the nonlinear model (NLM) simulations, we specified 3 km for horizontal decorrelation error length scales and all variables, except atmospheric forcing, which were set to 6 km. In vertical and all variables, we used uniform value of 30 m. In order to determine the prior variance, we integrated the NLM for nearly 6 years to calculate monthly climatological variances.

## 2.3. Observations

[9] In coastal regions, there are typically a limited number of available observations to constrain the greater dimensionality of the dynamics present. As such, we were unable to withhold data from the data assimilation system for an independent model to data comparison. This is one of the constraints that near-coastal systems impose as land proximity reduces the number of satellite derived products. In addition, due to the high resolution and the increased complexity of the physical dynamics, more constraints are required of the assimilation, so all observations are used.

### 2.3.1. ADCP Data

[10] ADCPs were deployed off the western shore of the coast of Oahu (Figure 1): two upward looking 1200 kHz ADCPs at 15 m (these are named ‘‘ADCP 9 northern’’ and

‘‘ADCP 8 southern’’) and two upward looking 300 kHz ADCPs at 80 m (‘‘ADCP 6 northern’’ and ‘‘ADCP 7 southern’’). The ADCPs measure current magnitude and direction throughout the water column at 1 m vertical resolution and 3 min sampling for shallow ADCPs and 8 m resolution with 10 min sampling for deep ADCPs. The instruments also measured water temperature near the bottom at each of the four sites. Water velocity data were collected near-continuously between 24 June 2009 and 25 August 2010 providing a total of 90,216 velocity records.

### 2.3.2. CTD Data

[11] The Hawaii Ocean Time Series (HOT) program [Karl and Lukas, 1996] routinely samples CTD profiles (from the near surface to 983 m depth) off the west coast of the island of Oahu (Figure 1, bottom). There were 132 available CTD profiles during the time frame of ADCP data collection. Although there are far fewer CTD data points when compared to the ADCPs, these CTD profiles provide valuable vertical density structure information not available from other types of instruments.

### 2.3.3. Satellite-Sensed SST Data

[12] SST data were provided by the Global Ocean Data Assimilation Experiment High-Resolution Sea Surface Temperature Level 2 Preprocessed database originating from Moderate Resolution Infrared Spectroradiometer (MODIS) sensors. The MODIS sensor is onboard the polar orbiting NASA AQUA and TERRA satellites that cross the equator twice a day. The swath data that were used have a 1.1 km spatial resolution and provide both the derived SST from combined spectral channels and the nominal error of the measurement. Because of the coastal application and sensor errors in the proximity of land, there was a limited amount of data available. During our experiment, we used

35,939 SST records, and the typical reported observation error was 0.25 K.

### 2.3.4. Observational Errors

[13] In this system, we did not assimilate raw data directly; instead, we preprocessed them in space and time to fit into the discrete model grid. We averaged all data from the same source that fall into the same model grid cell and time step and computed the variance as a nominal measure of the observation error estimate. For the experimental period, the averaged observation error estimate was  $0.25^{\circ}\text{C}$  for CTD temperature,  $0.002$  for salinity,  $0.34^{\circ}\text{C}$  for SST, and  $3\text{ cm s}^{-1}$  for ADCP velocity.

## 3. Numerical Model Experiment Setup

### 3.1. Nesting Procedure Setup

[14] We use a modeling system comprised of three one-way nested model grids as shown in Figure 1. The outermost model is at a 4 km resolution, covering the main Hawaii Islands (Figure 1, top) and is nested inside the global Navy Couple Ocean Model (NCOM) solution [Barron et al., 2006]. This model is forced at the surface by a local 6 km Weather Research and Forecasting (WRF) atmospheric model solution Nguyen et al. [2010]. Tidal forcing for 11 tidal constituents is provided by the Oregon State University TOPEX/Poseidon Global Inverse Solution (TPXO) database [Egbert and Erofeeva, 2002] added to the NCOM derived boundary conditions. 4D-Var state estimation technique is used to further improve the state of this outer model [Matthews et al., 2012]. The model is capable of reproducing dynamics at the scales of  $O(10\text{ km})$  and in our case is used to provide boundary conditions for a finer scale Oahu model with variable resolution of  $\sim 2500\text{ m}$  in the deeper part of domain and  $\sim 600\text{ m}$  in the coastal regions of Oahu (Figure 1, bottom). This Oahu model is forced with a 2 km resolution WRF model and also assimilates available observations via 4D-Var. This refinement grid is a significant improvement compared to the outer model in the resolution of the steep bathymetry of the region and representing shallow features around the island of Oahu [Janeković and Powell, 2012]. Embedded within the intermediate grid, is the model of this study, with a variable resolution of  $\sim 1\text{ km}$  along the deep, western boundary and  $\sim 200\text{ m}$  along the coast (Figure 1, bottom). It is forced hourly with further nested WRF model having resolution of 1 km.

[15] The nesting procedure with a state estimation system requires additional care when propagating boundary conditions from a parent to a child model. If boundary conditions are a component of the control vector, the nested circulation could become decoupled from the parent, even the deterministic flow such as the barotropic tides. To prevent this, we used a combined approach of applying barotropic tidal information as a separate spectral forcing (removed from the BCs [Janeković and Powell, 2012] to keep it independent of the control vector), and we limited the frequency of three times per day at which perturbations to the BCs,  $\delta\mathbf{x}_{\Omega}(t)$ , could be made.

[16] ROMS is a terrain-following coordinate model and the depths of the levels vary in space and time.

This is particularly advantageous for near-coastal regimes; however, problems can arise in the regions of steep bathymetric change (large vertical gradients over short horizontal distances). These steep gradients create pressure-gradient errors [Shchepetkin and McWilliams, 2003] that must be reduced by smoothing the bathymetry. In our case, we minimize the change of the original bathymetry in order to keep modeled depths similar to the actual using a novel linear programming technique [Sikirić et al., 2009]. As a result, the model bathymetry is a slightly smoother than the reality. This is true for any model due to discretization, but the additional modifications mean that the ADCP depths and model grids do not match precisely. Those differences will alter the amplitude and direction of the barotropic tide as compared to the observations. The model integration without assimilation has a typical error for major semi-axes of  $7.5\text{ cm s}^{-1}$ , minor semi-axes of  $0.3\text{ cm s}^{-1}$ , and inclination of  $12.7^{\circ}$  for the barotropic  $M_2$  tidal ellipse parameters. The mean absolute bathymetric difference between the model grid and the actual depth of the ADCPs is 34 m. However, the better comparison is found for northern ADCPs which have smaller depth and tidal discrepancy. ADCP 8 was deployed at 14 m depth while the model location is 95 m deep, and it compares least favorably with errors of  $12.5\text{ cm s}^{-1}$  for major and  $26^{\circ}$  for inclination errors. If omitting ADCP 8 from the calculations, the overall error values are smaller (major semi-axis is  $6\text{ cm s}^{-1}$ , inclination  $8^{\circ}$ , and mean absolute depth difference between model and ADCPs 6, 7, and 9 is 19 m). As a consequence, we first remove the barotropic tidal information from all ADCP observations and apply the barotropic tides from the model prediction of the flow. These adjustments to the observations were to prevent model corrections to the barotropic tide to account for errors in the bathymetric representation. Our goal is to match the baroclinic and surface circulation including internal tides, wind-induced layer, submesoscale, etc., to understand which dynamics control the circulation along the western Oahu coast.

### 3.2. 4D-Var Model Setup

[17] In this study, the finest resolution model is used to examine the one-way nesting capabilities inside the 4D-Var estimation scheme. Clamped baroclinic boundary conditions for temperature, salinity, and 3D velocity, Chapman [1985] for free surface, and modified Flather type [Marchesiello et al., 2001] for barotropic momentum are used. Surface fluxes between the ocean and atmosphere are computed via the COARE algorithm [Fairall et al., 1996] using information from the local WRF atmospheric model. Third order unbiased advection schemes are used in the horizontal, while fourth order centered are used in the vertical. For vertical turbulence closure, we used 2.5 level scheme of Mellor-Yamada [Mellor and Yamada, 1982], while at the bottom, we used the standard quadratic bottom friction formulation. A time step of 60 s is used to ensure the stability of the integration during the whole period of experiment.

[18] The two primary assumptions of variational state estimation are that increments made to the system are small compared to the dynamics, and nonlinear effects within

data assimilation window are also small. The latter assumption was tested by generating an ensemble of 40 orthonormal perturbations and integrating them separately via the TLM and the NLM. Comparison of the TLM and NLM ensemble root-mean-square differences and correlations showed consistency between them over 4 days of integration.

[19] To understand the limits of the initial state on predictability, we examine the persistence of perturbations made to the initial conditions by integrating the model using fixed ICs to generate a “true” circulation estimate. We then integrate an ensemble of random climatological states using the same BCs and FFs. The integrations are compared to the “true” circulation using correlation in time for each of the state variables (temperature, salinity, free surface, velocity) at every grid cell, in order to determine the time required to force the circulation back to the unperturbed trajectory. On average, the system returns to the unperturbed state after only 2.5 days due to the BCs and FFs. We expect that boundary conditions and surface forcing are more important as assimilation control vectors than the ICs over the 4 day assimilation window.

#### 4. Results and Discussion

[20] We assimilated all the available observations from 3 August 3 2009 until 17 July 2010 using 88, 4 day assimilation window cycles. Based on these simulations, the general circulation along the western coast of Oahu is predominantly along-shore, and strongly modulated with diurnal and semidiurnal tidal dynamics. The  $M_2$  tidal constituent is the most dominant, which corresponds with the results of *McManus et al.* [2008]. This regular, oscillatory motion is further modified by both the flow along topographic features as well as by event-driven mesoscale dynamics.

[21] During the minimization procedure, we used 15 iterations to reach an asymptotic value for the cost function,  $J$  (equation (1)). During the assimilation procedure setup, we experimented with the number of iterations and found that for the test case, little improvement was found after 15 iterations. Upon completion of the experiment, we calculated the mean, normalized  $J$  after each iteration as shown in Figure 2. Over the entire period, the typical linear minimization reduced the cost function by nearly 88%. However, despite the prior test for linearity, oftentimes the circulation was highly nonlinear over the 4 day cycle. As such, the mean true, nonlinear cost function was reduced on average to only 43%. This reveals the difficulty in coastal assimilation problems. We could shorten the time window; however, the number of available observations would be greatly reduced; hence, we chose a compromise in which the linear minimization did not fully realize the nonlinear circulation. Overall, the nonlinear flow was still significantly reduced, and examining each observation type, we find that—on average—the reductions were 29% for CTD temperature, 38% for CTD salinity, 43% for ADCP alongshore component,  $-34\%$  for ADCP cross-shore component (more on this increase below), and 31% for SST.

[22] Useful way to gauge performance of the data assimilation is to define a residual error between model estimate and observations, scaled with observation errors:

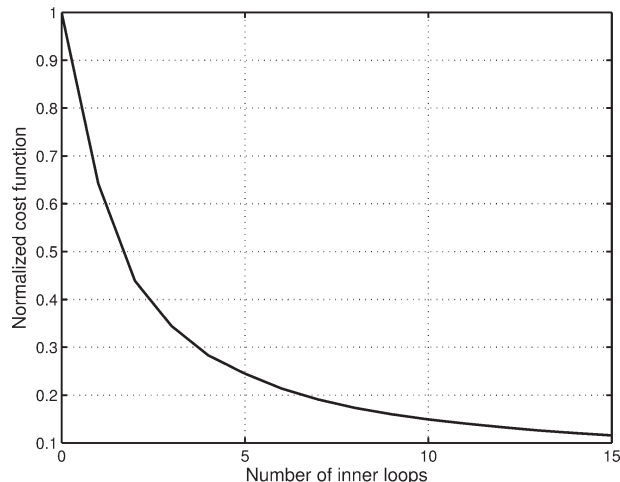


**Figure 2.** The mean, normalized linear cost function,  $J$ , value after each iteration over the entire assimilation experiment. During the linearized minimization (using the TLM), the  $J$  was reduced by nearly 88% by the end of the minimization. Due to the strong nonlinearity in the coastal flow, the actual NLM  $J$  was reduced—on average—43%.

$$E = \left[ (\mathbf{y} - \mathcal{H}(\mathbf{x}_a(t)))^T \mathbf{R}^{-1} (\mathbf{y} - \mathcal{H}(\mathbf{x}_a(t))) \right]^{\frac{1}{2}} \quad (2)$$

where  $\mathbf{x}_a(t)$  is the *posterior* (or analysis) solution after data assimilation. In our case, the observation vector,  $\mathbf{y}$ , was composed of CTD temperature and salinity, directional components of ADCP currents and SST data.

[23] The  $E$  values provide a unitless ratio between the model and observation and the observational error:  $E > 1$  states that the residual is greater than the uncertainty in the observation, while  $E < 1$  means that the residual is within the error bounds of the observation. The mean residual errors,  $\bar{E}$ , over the experimental period for the posterior are favorable (Table 1), showing reduced values when compared to the prior. The average reduction of the  $\bar{E}$  before and after 4D-Var varies between 13.6% for CTD temperature to 34.1% for ADCP alongshore component of currents with the exception of increased value for the ADCP cross-shore component ( $-11.8\%$ ). The root-mean-square error (RMSE) shows similar result with CTD temperature improved by 24.4%, ADCP along-shore improved by

**Table 1.** Statistical Values for the Mean Residual Error ( $\bar{E}$ ), the Root-Mean-Square Error (RMSE), and the Mean Absolute Error (MAE) Between Model and Observations for Both the Prior and Posterior<sup>a</sup>

	Temp	Salt	Velocity (Along)	Velocity (Cross)	SST
$\bar{E}$ prior	1.91	4.29	0.44	0.17	0.43
$\bar{E}$ posterior	1.65	3.44	0.29	0.19	0.30
RMSE prior	1.31°C	0.23	9.9 cm s <sup>-1</sup>	4.0 cm s <sup>-1</sup>	0.34°C
RMSE posterior	0.99°C	0.19	7.1 cm s <sup>-1</sup>	4.5 cm s <sup>-1</sup>	0.24°C
MAE prior	0.96°C	0.19	7.7 cm s <sup>-1</sup>	3.0 cm s <sup>-1</sup>	0.25°C
MAE posterior	0.78°C	0.15	5.1 cm s <sup>-1</sup>	3.4 cm s <sup>-1</sup>	0.18°C

<sup>a</sup>Temp and salt are data from the CTD casts, velocity along- and cross-shore are from the ADCPs, and SST are from MODIS.

28.3% and SST by 29.4%. Similarly, the mean absolute errors (MAE) gives absolute bias, which is reduced by 18.7% for CTD temperature and ADCP along-shore reduced by 33.8%.

[24] Analyzing raw ADCP and corresponding model realizations at the ADCP locations reveals a polarization of the flow. Rotating the ADCP data into the modeled along-shore and cross-shore coordinate system identifies that 94% of the total kinetic energy is in the alongshore direction. The power spectrum of the ADCP data (Figure 3) clearly show the majority of energy in the semidiurnal and diurnal tidal bands with the energy in the alongshore currents more than an order of magnitude greater than the cross-shore. Because the cross-shore ADCP currents are small and of similar magnitude to the prescribed observation errors, their relative impact within data assimilation is minimal, and it is why the RMSE, MAE,  $\bar{E}$  values worsen with the

assimilation. In assimilating the ADCP data, we pre-processed the data such that it is vertically binned into the model coordinates, averaged into 30 min intervals, and removed the barotropic tides to add the modeled barotropic tides as described earlier. Surface waves due to remote swells or wind induced dynamics were not included in the model simulation. The average correlation between along-shore modeled currents and the preprocessed ADCP data is 0.91 over the year.

[25] ADCP data are important for measuring the state of the ocean; however, they provide information at a single location that may not be representative of the whole domain. In order to provide context, we rely upon the model dynamics to propagate the informational connection between all observations and the modeled domain. Mean surface circulation from the assimilative model (Figure 4) shows flow directed toward the coast in the central region

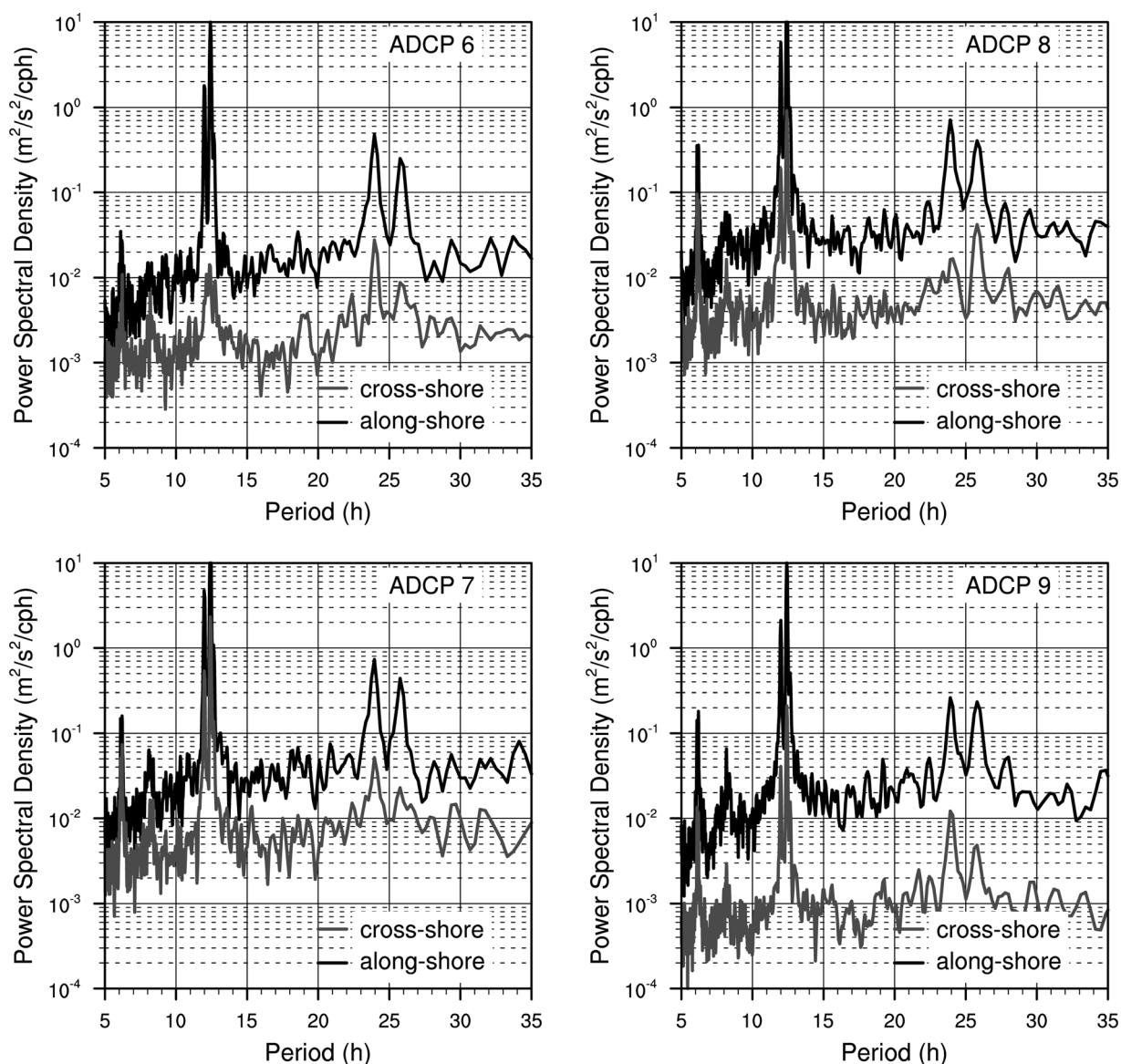


**Figure 3.** Power spectral density of ADCP vertically integrated currents, rotated onto model along-shore and cross-shore directions. The alongshore flow is nearly 2 orders of magnitude larger than the cross-shore with spectral peaks at the diurnal and semidiurnal tidal frequencies.

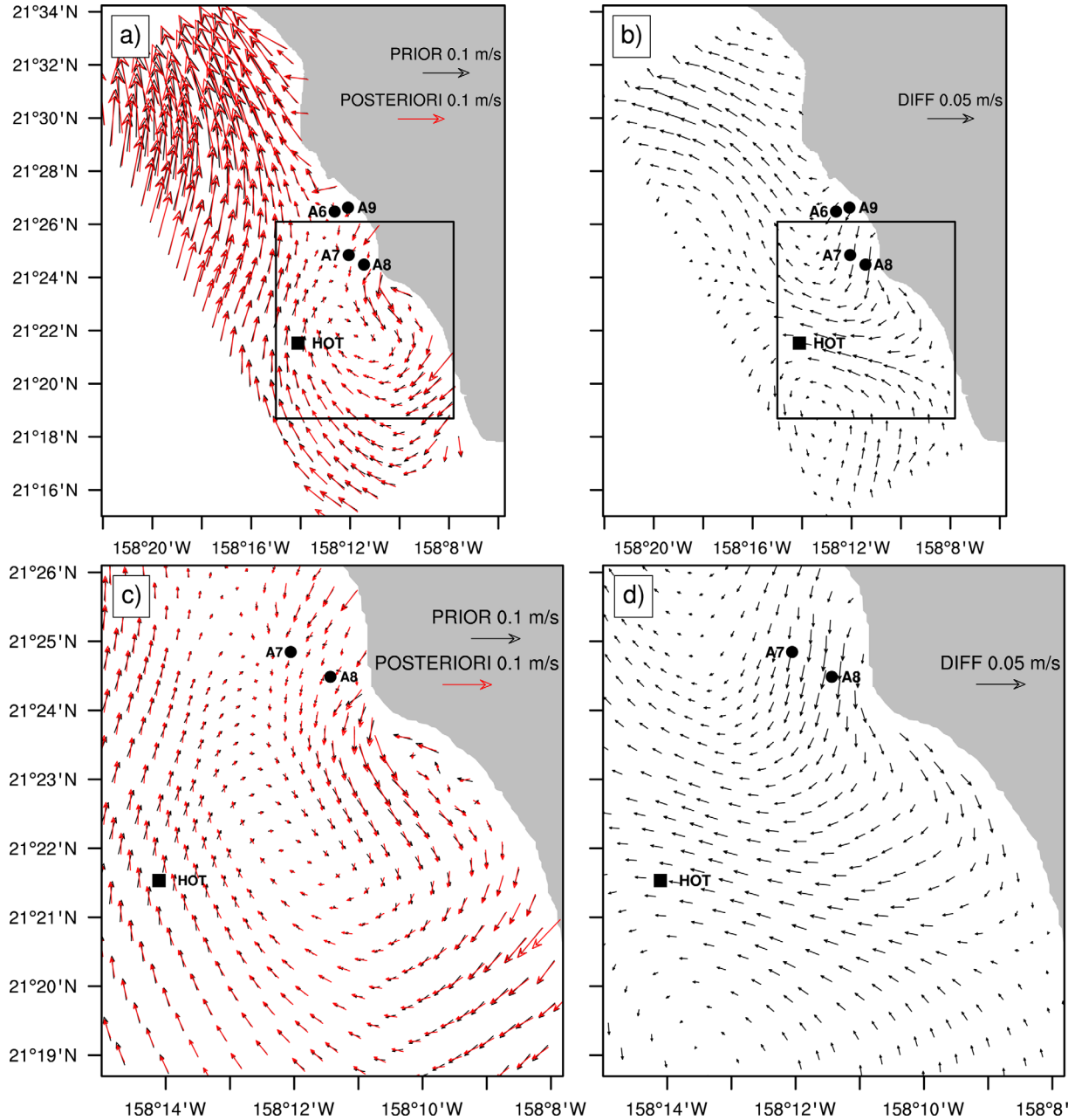


**Figure 4.** (a) Time mean surface velocity fields for the experimental year from 4D-Var prior (black) and posterior (red) solutions. (c) Magnification of surface velocities in the southern part of the model domain. (b and d) The time mean surface velocity differences between the posterior and prior solutions for the same regions. ADCP locations are marked with black dots and corresponding names (A6–A9), and the HOT CTD location is marked with black square and label.

where the ADCP stations were deployed, with bifurcation and enhanced flow along the coast at the northern and southern branches. The southern branch flows along the coast to the southeast and is characterized by stronger rotation in the flow field (Figure 4, bottom) as a consequence of interacting with the flow of the strong Hawaiian Lee Current (HLC—a mean ocean circulation in the leeward side of Hawaiian Island chain, see *Lumpkin* [1998] and *Lumpkin and Flament* [2013]), that flows past the southern tip of the island of Oahu. The effect of the data assimilation corrections is evident in the right-hand side of Figures 4b

and 4d. The assimilation corrections to the surface current system enhance bifurcation and along-coast flow directed toward the north and the south from the central region.

[26] Seasonality of the coastal current system during the 2009–2010 year is more pronounced in surface layers where atmospheric forcing through atmosphere-ocean boundary layer dynamics has more effect. In the winter time, surface flow is the strongest and directed to the northwest, as a direct consequence of strong southerly winds during the weakened Trade Wind system (Figures 5a and 5c). Even in the monthly averaged currents, these winds

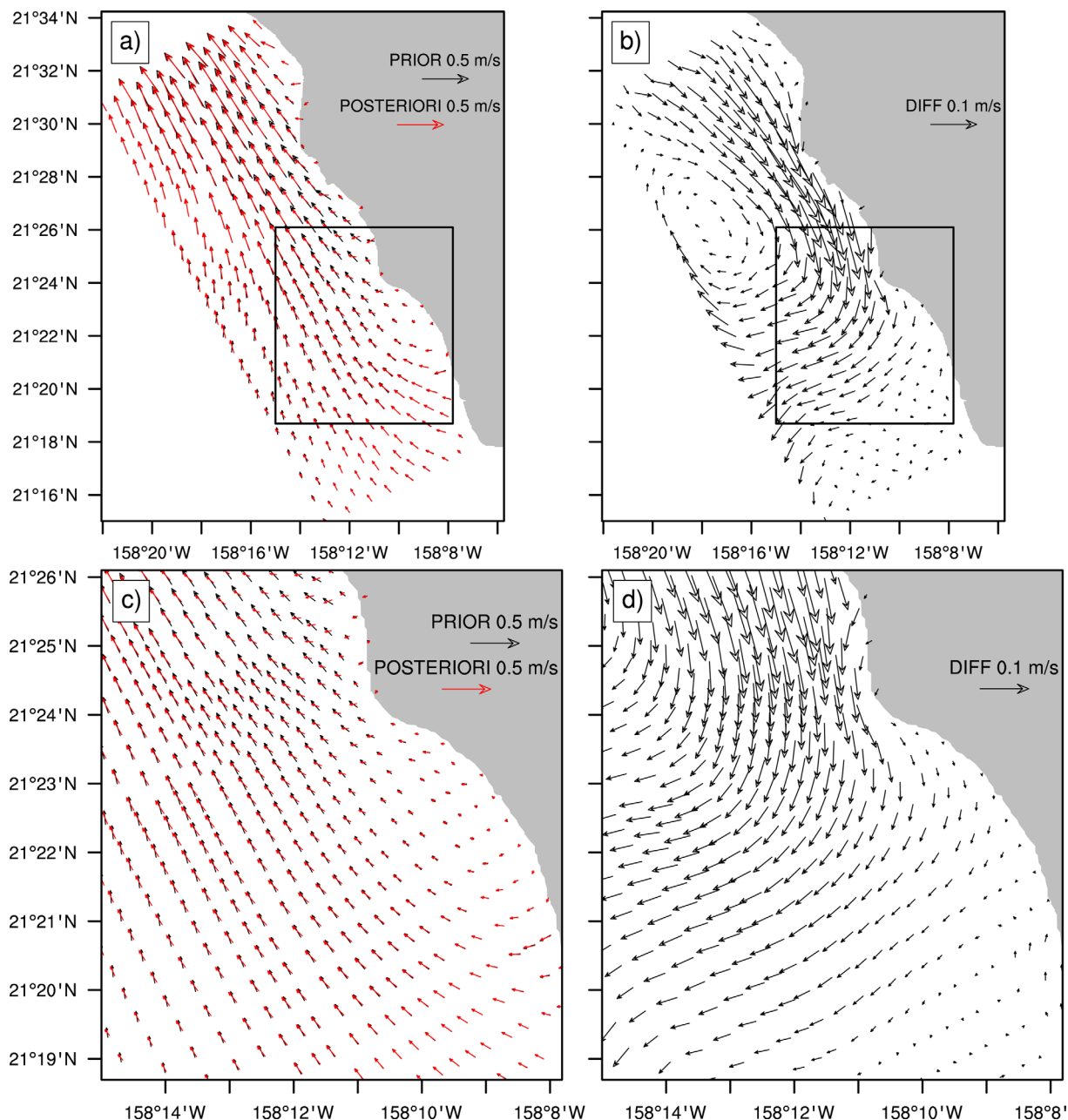


**Figure 5.** (a) Time mean surface velocity fields for the March 2010 period from 4D-Var prior (black) and posterior (red) solutions. (c) Magnification of surface velocities in the southern part of the model domain. (b and d) The time mean surface velocity differences between the posterior and prior solutions for the same regions.

drive water masses along the Western Oahu coast toward the north. Examining the difference between the posterior and prior estimates (Figures 5b and 5d) shows enhanced curl in the surface flow as a direct consequence of the data assimilation corrections. During the Easterly Trade Winds of the summer/autumn, the western coast region is in the island-blocked wind shadow resulting in weak currents of the opposite direction (not shown).

[27] Variations in the temperature field at the surface are small, between 24°C and 28°C, typical for the region. In the vertical, temperature shows stable temporal profiles with the mean yearly values at the surface near 26°C and a

thermocline depth of  $\approx 200$  m. Mean variability in vertical temperature field for August 2009–July 2010 period has maximal values up to 1.3°C found at the thermocline depth due to heaving of the thermocline by internal tides (or other mesoscale features).

[28] The circulation was altered by variations in the ICs, BCs, and FFs. In the case of forcing, the largest corrections were applied to the wind stress in the lee of the Oahu Island. This correction is not surprising because mean wind stress is at a minimum in the central west coast of Oahu (Figure 6) due to reduced wind behind the high mountains. The variability in the atmospheric model may not be

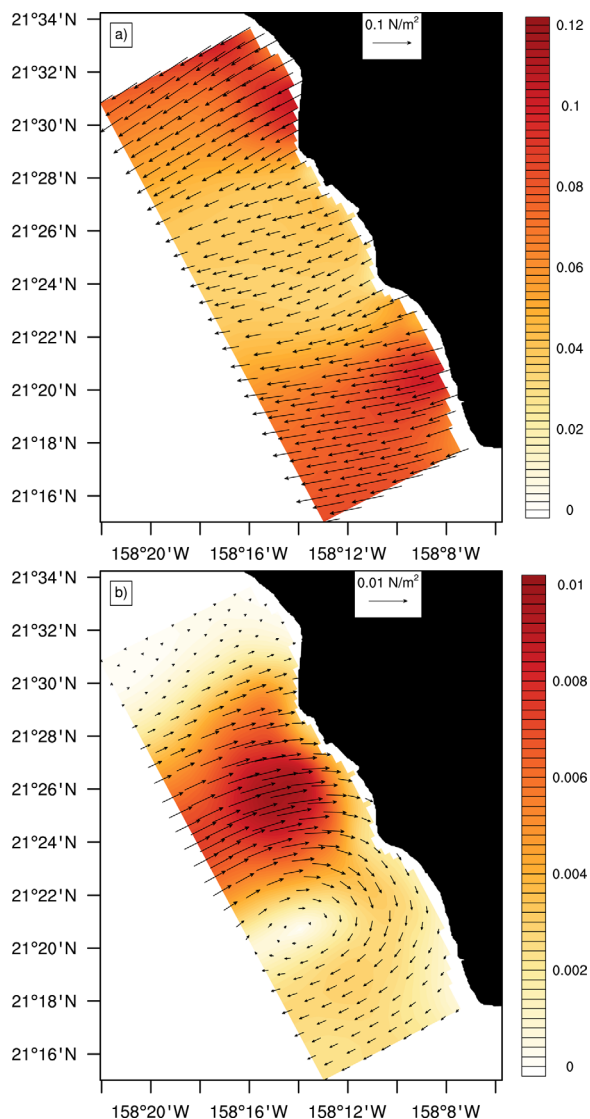


**Figure 6.** (a) Time mean surface wind stress forcing magnitude and direction used during the 1 year experiment. (b) The time mean wind stress forcing corrections applied by the 4D-Var procedure to generate the posterior solutions. Note that the corrections are an order of magnitude smaller than the forcing, and on average, the 4D-Var slows the wind forcing in the central portion of the domain.

adequate to represent the steep terrain of the Waianae Mountains ( $\approx 1200$  m) in sufficient detail, consequently, overestimating wind in the lee of the island [Nguyen *et al.*, 2010]. The adjustments in the wind stress field are not only due to the representation of the atmospheric model estimate of the wind (and, consequently, wind stress), rather wind adjustment is an effective mechanism for the 4D-Var modeling system to reduce the residual with respect to the observations through time.

[29] Conversely, the strong northeasterly trade winds to the northern and southern tips of the island are responsible for inducing both vorticity and Ekman pumping [Chavanne *et al.*, 2002]. This is analogous—but a slightly different atmospheric regime—to the lee of the big island of Hawaii, where high mountains interrupt the wind field and create an

island wake effect, with counter current flow toward the western coast [Xie *et al.*, 2001]. In the case of Oahu, the Waianae Mountains are not tall enough to pierce the trade wind inversion layer; however, they influence wind flow significantly [Nguyen *et al.*, 2010]. The mean perturbation to the surface wind stress due to assimilation is 10% of the mean surface wind stress itself. Wind stress is reduced in the central waters off the western side of Oahu, while it is increased in the south resulting in enhanced eastward flow (Figures 4b and 4d). As a consequence, the island wake dynamics are altered; however, the fine model grid does not extend far enough to the west to capture the full wake. The island wake coastal boundary layer dynamics are fully resolved including the bifurcation point. A similar experiment for the region of Central California [Broquet *et al.*, 2011] found when surface forcing adjustments were made, the assimilation system yielded more realistic upwelling dynamics.

[30] Comparing our wind field with the QuikSCAT-derived winds is not feasible due to its coarse resolution, while this study is focused on the coast. On the larger-scale, similar results to ours, were found around Hawaii with reductions in wind stress in the lee of the island chain and increasing in the southern and northern regions by 5–10% [Matthews *et al.*, 2012]. The net effect of the modified winds on the mean surface dynamics is subtle (Figure 4), with similar prior and posterior model trajectories. Small relative differences are found in the regions of weaker currents (Figure 4, bottom) and relative large surface wind stress corrections. Examining the mean heat flux corrections (Figure 7) made during the whole experiment by the data assimilation system, we find an increase of heat flux into the ocean in the northern part of the domain with

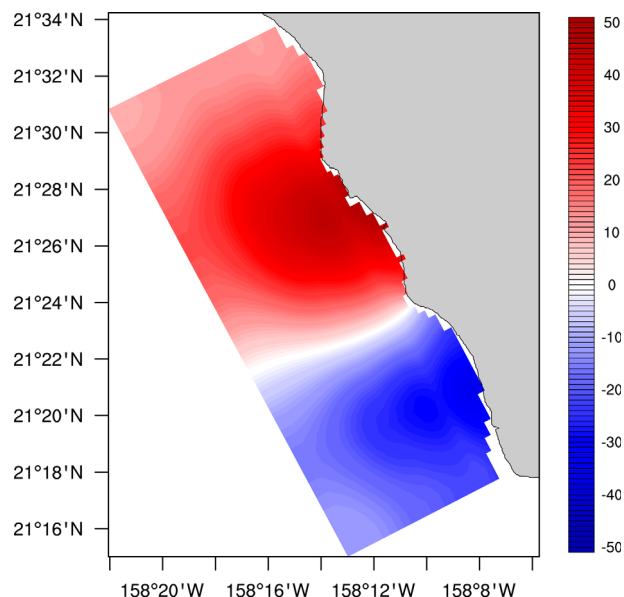


**Figure 7.** Time mean surface heat flux forcing corrections applied by the 4D-Var procedure to generate the posterior solution in  $\text{W m}^{-2}$ . On average, the northern portion of the domain received slightly increased warming (peak heat flux during the afternoon is over  $800 \text{ W m}^{-2}$ ), while the southern portion was cooled.

increments up to  $50 \text{ W m}^{-2}$  and reductions in the southern part with increments of  $-20 \text{ W m}^{-2}$ .

[31] There is a negligible mean warm bias in the model of  $0.01^\circ\text{C}$  compared to the SST, which indicates that atmospheric corrections are primarily required to adjust the momentum. The mean wind stress (Figure 6) and heat flux (Figure 7) corrections show a similar pattern; however, they are not compensating each other as one may expect. In the central region of the lee of the Oahu Island, the heat flux corrections input more heat into the ocean and at the same time reduce the wind stress making surface heating process more efficient.

[32] Fresh water corrections are small (not shown) with positive increments (freshwater input) at the southern part and negative at the northern (freshwater outputs), opposite to heat flux correction pattern. These two mechanisms are working together, where the data assimilation system is reducing heat flux to the ocean (negative heat flux increments) we have at the same time positive salt flux increment (i.e., net evaporation). This corresponds with earlier observations [McManus *et al.*, 2008] where the heat flux and fresh water input vary inversely during the seasons.

[33] This is true for the mean state; however, when winter atmospheric dynamics are more energetic, as in the case of March 2010 (when the winds were strongest during the modeled year) differences are noticeable even on monthly averaged scenes (Figure 5, central coastal region). Comparing surface current magnitudes for the prior ( $|\mathbf{u}|_b$ ) and posterior ( $|\mathbf{u}|_a$ ) model simulations reveal a  $5 \text{ cm s}^{-1}$  root-mean-square difference, which is 20% of the prior solution magnitude. To understand individual contributions from each control vector to the surface dynamics, we focus on 15–19 March 2010 period. In that period, wind forcing was strong, winds stress correction was the largest, and there are notable difference between the prior and posterior surface currents, providing an excellent test case to understand the individual contribution of corrections made via data assimilation system. We performed five experiments to examine the nonlinear effects of adjusting each of the ICs, BCs, and FFs. The five experimental NLM integration are defined as

[34] E1: unperturbed prior integration,

[35] E2: full posterior integration with ICs, BCs, and FF adjustments,

[36] E3: prior integration with BCs from E2 to examine the effect of the boundary control vector,

[37] E4: prior integration with ICs from E2 to examine the effect of the initial condition control vector,

[38] E5: prior integration with atmosphere adjusted forcing from E2 to examine the effect of the wind stress control vector.

[39] The greatest difference in the surface currents between E1 and the others is found—unsurprisingly—with E2 (Figure 8). The combined perturbations enhance the alongshore southeastward circulation near the coast, while the off-shore is adjusted in the opposite, northwestward direction (Figure 8a). For the individual experiments E3–E5, the boundary control (E3) contributes the most significant change to the circulation (Figure 8b), accounting for 45.5% of the total E2-E1 difference. The initial state control (E4), as shown earlier using the ensemble of perturbed initial states, exhibits short persistence and produces small

control effect accounting for only 16.8% difference. The atmosphere-ocean fluxes and wind stress control (E5) introduce the smallest portion (8%) of overall control, but is important in the central region of the domain (Figure 8d). The wind controls the flow toward the lee of the island, as well as coastal flow in the southwest direction. Even the wind stress correction for the case is the largest within the whole studied period, its effect on the surface circulation is still almost 3 times smaller than BC adjustment.

[40] These results indicate that the coastal dynamics in the lee of Oahu are dominated by larger-scale signals from the Hawaiian Lee Current to the south and, more weakly, the North Hawaiian Ridge Current (NHRC) to the north of the domain that are enhanced by the wind-wake effects. This is unsurprising as the primary exchange of HLC and NHRC waters is through the Kauai Channel connecting Oahu to Kauai in the west [Lumpkin, 1998]. Furthermore, variability of the wind-wake driven Hawaiian Lee Counter-current [Lumpkin and Flament, 2013] significantly alters the HLC and its eventual strength in the lee of Oahu.

[41] As shown in Figure 3, the tides are the dominant energy of the region. For the modeling experiments, the BCs are responsible for propagating this energy into the area. There is no significant barotropic-to-baroclinic tidal conversion occurring within the fine model domain because little of the steep, supercritical Kaena Ridge is present in the fine model domain. These baroclinic tides are imposed by the parent models and propagate into the fine model domain. During the estimation procedure, the density field changes the baroclinic tide waveguide; therefore, it should be expected that after some time, the BCs updates will impose the greatest control on the baroclinic flow. In order to estimate the change to the flow of the baroclinic tides, we compute vertically integrated time-mean baroclinic energy flux ( $F$ ) defined as

$$F = \int_{-H}^{\eta} \langle p'u' \rangle_{\theta} dz \quad (3)$$

where  $\langle \cdot \rangle$  is time mean expectation,  $p'$  is baroclinic pressure perturbation,  $u'$  is baroclinic velocity perturbation,  $H$  is the water depth,  $\eta$  is the sea surface height.

[42] As shown in Figure 9, the energy flux is similar for the E1 and E2 solutions both in magnitude and direction, exhibiting the dominant north to south propagation pattern [Merrifield and Holloway, 2002; Nash *et al.*, 2006; Carter *et al.*, 2008; Chavanne *et al.*, 2010; Janeković and Powell, 2012]. In the fine-scale model solution, we can see that the near-coastal southern branch of  $F$  is directed to the north in the opposite direction to the main southward stream. This fine-scale feature is not seen clearly on the previous large-scale model solutions [Carter *et al.*, 2008; Janeković and Powell, 2012]. The origin of this energy flux is the coastally trapped internal tides that propagate from south Oahu that is captured by the nested models [Alford *et al.*, 2006].

[43] Furthermore, to investigate alongshore vertical structure of baroclinic energy flux, we computed temporal averaged fields through a cross-shore transect located in the middle of model grid as shown by the green line marked at Figure 9 (left). The posterior solution (E2) is similar to the prior (E1) with slightly reduced flux in the western (off-shore) region and depths up to 200 m (Figure 10). In

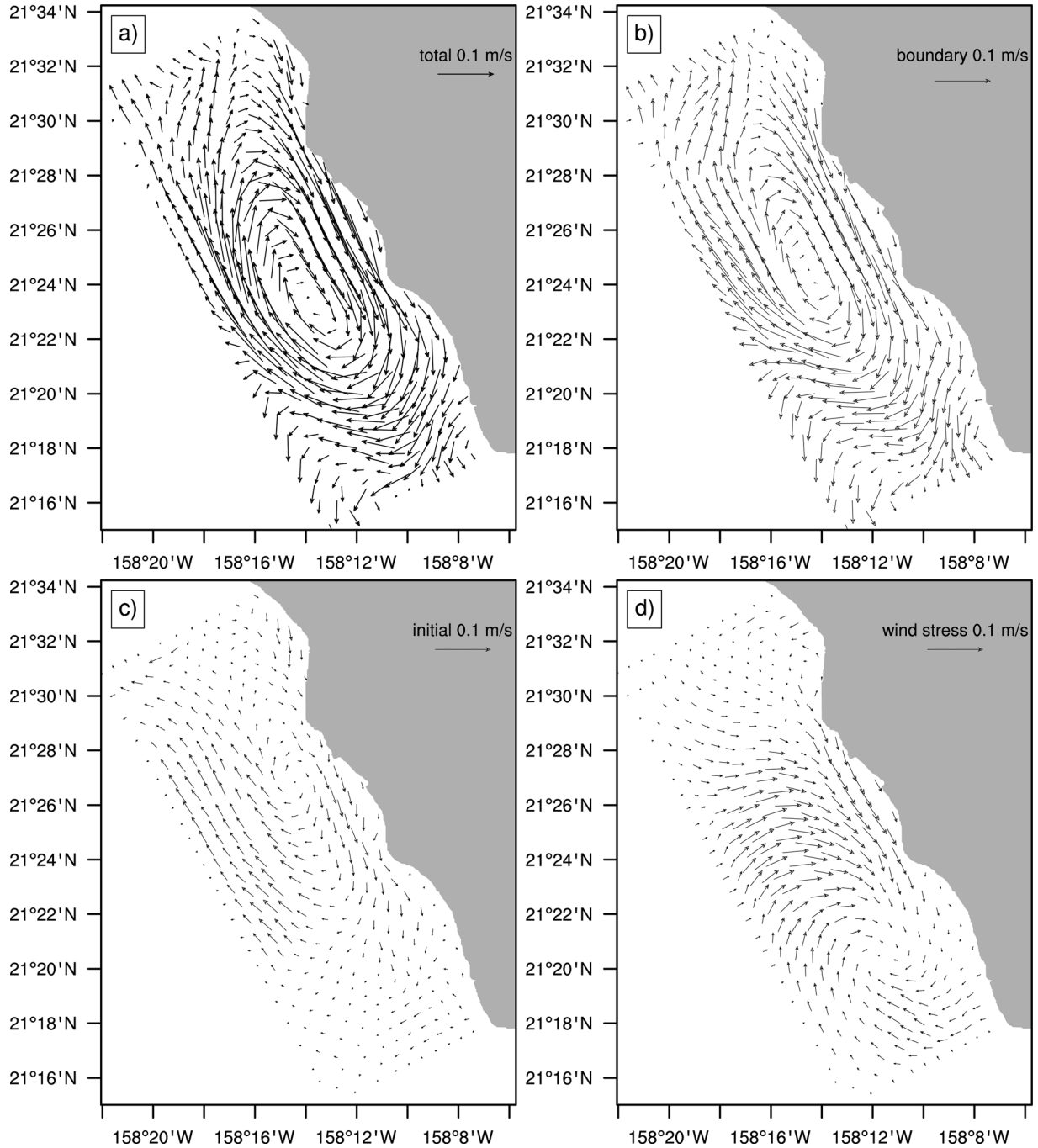


**Figure 8.** Time mean surface velocity differences for 15–19 March 2010 between: (a) E1 prior and E2 posterior; (b) E1 and E3 (boundary condition adjustment only); E1 and E4 (initial state adjustment only); and, (d) E1 and E5 (surface forcing adjustment only). The similarity between (a) and (b) illustrate that the BCs are the dominant control for the experiment.

coastal region, there is baroclinic energy flux directed to the north, as seen before on Figure 9, but mostly bounded in the surface layer up to depth of 100 m. In the case of E2, this coastal northward flux is more extended off the coast than in background solution, E1.

[44] We compute the dominant, north-south directed, baroclinic energy flux, every 2 h over each of the March experiments (E1-E5) to examine the temporal contribution of each control vector. This information is important for

determining the adjustments that have the most (or least) effect on the baroclinic energy flux determined from E2. Calculating the correlation between the baroclinic energy flux for E2-E5 with the prior solution E1 provides the temporal and individual importance of 4D-Var adjustments (Figure 11). The spatial correlation between the two fields is computed at each saved model time step; hence, we show the spatial correlation every two hours from the beginning of the experiment. The prior is not the true flux;

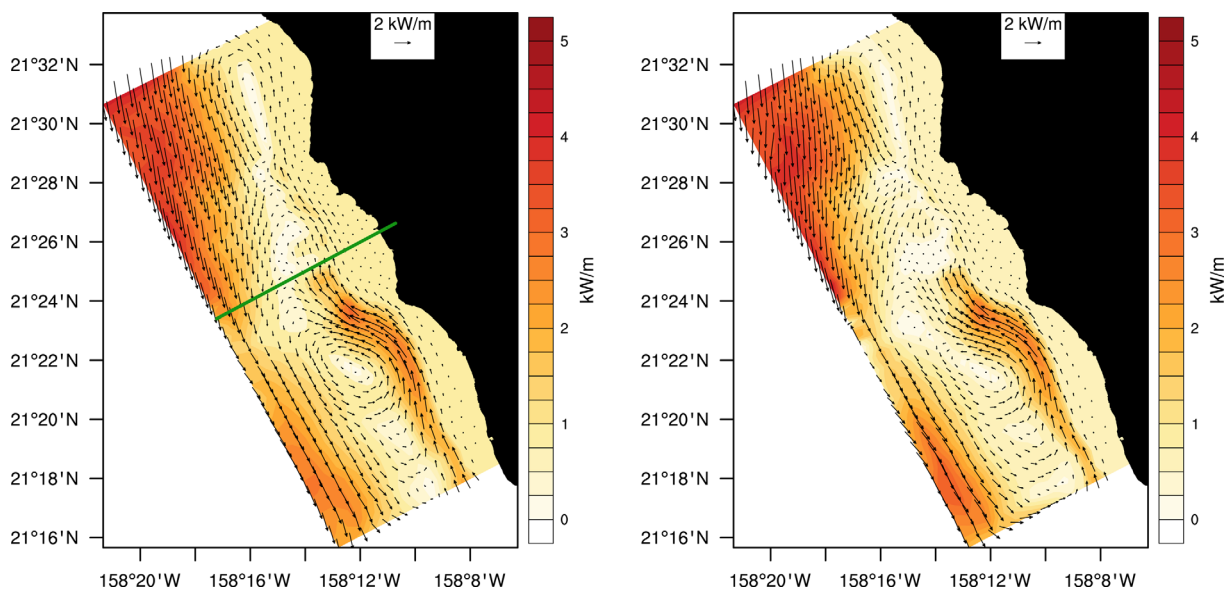


**Figure 9.** Depth integrated, time-mean baroclinic energy flux ( $\text{W m}^{-1}$ ) for the (left) E1 and (right) E2 experiments. It is important that the assimilation did not significantly alter the incoming energy flux. Transect used for Figure 10 is marked with a green line in the left panel.

however, it is a useful, fixed reference to gauge how the various controls altered the baroclinic flux. As such, high correlation is not indicative of a positive result, rather high correlation illustrates that the control had little affect in

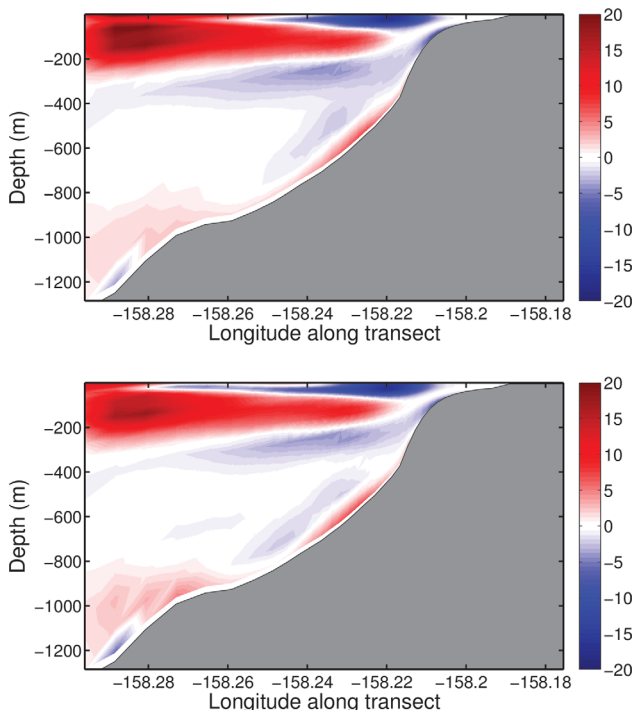


**Figure 10.** Vertical transects of time-mean baroclinic energy flux ( $\text{W m}^{-2}$ ) for the (top) E1 and (bottom) E2 experiments. Although the vertically integrated flux is consistent, the stratification is altered, providing slightly different distribution of energy. Transect is located in the middle of the model domain in the offshore direction (denoted by the green line in the left panel of Figure 9).

controlling the posterior baroclinic flux. We find the following:

[45] (i) Over the first semidiurnal cycle, the density field waveguide (as determined by the ICs in E4) most contributes to the analysis (E2), after which the fluxes return to the E1 case. In other words, in the beginning, the ICs adjustments (E4) are highly correlated with full 4D-Var solution (E2) suggesting that during the initial 12 h, the ICs provide the most important control. After this initial period, the contribution decays in time approaching the unmodified, prior state solution (E1) as the ICs control quickly dissipates.

[46] (ii) After 12 h, the incoming flux from the BCs (E3) accounts for the difference between the posterior solution (E2) and the prior (E1), and after 1.5 days, it is highly correlated with E2. This shows that the baroclinic energy flux patterns are controlled by energy originating away from the west Oahu propagated via BCs. As the internal tides are

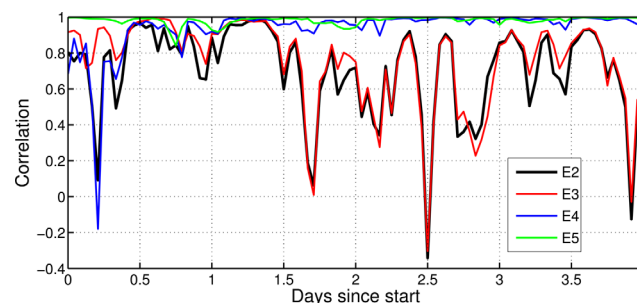


**Figure 11.** Correlation for model output times and baroclinic energy flux along the transect (as in Figure 9). Correlation is computed between the prior solution (E1) and (black) 4D-Var posterior, E2; (red) BCs control, E3; (blue) ICs control, E4; and, (green) wind stress control, E5. The higher the correlation with E1, the less control a particular field has on the baroclinic energy flux.

generated on Kaena Ridge and propagate into the domain, this result should not be surprising.

[47] (iii) The wind control vector part (E5) has no effect on the baroclinic energy flux estimate of the analysis, showing high correlation with baseline solution—E1 experiment.

[48] Based on these results, it is evident that the most important overall effect on the change of baroclinic energy flux is introduced via BCs (E3), locally adjusted processes within domain are of secondary importance.

## 5. Conclusions

[49] In this work, we examine the results from 4D-Var state estimation experiments in a triple, one-way nested model configuration to identify the dynamics that control the circulation off the western coast of the island of Oahu, HI. During the yearlong experiment, each nested model used 4D-Var with model/region specific available observations. Within the nesting, special care was taken for spectrally specifying barotropic tides because boundary conditions were part of the control vector, and we aimed to prevent altering the barotropic tidal flow. This did not prevent the dynamics of the internal tides within the fine-scale model that are introduced via the boundary conditions. During the experiment, we used all available data from ADCP, CTD, and SST to better constrain the highly dynamical coastal system. The size of the grid determined the number of observations available for assimilation, with coastal grids lacking significant satellite coverage because of land contamination.

[50] Based on the model results and available ADCP observations, the general circulation along the western coast of Oahu is along-shore and strongly modulated by the tides with  $M_2$  dominating. The flow is further modified with atmospheric interactions through the surface momentum/heat exchange that generate a corresponding response in the ocean—an island wake effect. During a 13 month period, from July 2009–August 2010 the correlation between model state estimated solution and ADCP observations was 0.91. Highly polarized flow in the alongshore direction contains 94% of total kinetic energy, and the 4D-Var procedure was able to significantly reduce the residual error. On the other hand, cross-shore component is an order of magnitude weaker and of similar value to the prescribed observation error, providing no net effect on the assimilation.

[51] This dynamic region is characterized with strong internal tides originated from the conversion site at Kaena Ridge, and is located between HLC at the southern and NHRC at the northern portions of the model domain. The dynamics produced at Kaena Ridge lie outside of our fine-resolution nested domain and are introduced through the BCs. Energy advected from Kaena Ridge, as well as HLC and NHRC, into the fine nested domain is found to be the dominant control vector, while the local dynamic produced with atmosphere is controlled by the atmospheric forcing control vector.

[52] The baroclinic tides follow established energy paths and are altered by the initial state—via the density waveguide—only within the first semidiurnal cycle. After nearly 13 h, all baroclinic tidal influences originate away from the coastal lee. Inside our domain, there is no significant barotropic to baroclinic energy conversion; hence, all baroclinic

dynamic is controlled through the BCs imposing dynamics generated outside the nested model. Even during trade-wind periods and the largest wind stress correction, these external dynamics adjustments (as modified by the BCs control vector) are the most important, and account for 45% of the total corrections made via data assimilation system to the surface circulation. The winds control 8% of the corrections made via data assimilation system; however, over the entire experimental period, the wind stress is reduced on average  $\approx 10\%$ . This suggests that care must be taken with the atmospheric model solutions as they may overestimate wind conditions. The initial state of the model has little effect for the corrections made via data assimilation system on the surface circulation due to the short persistence in the region, and the ICs account for little less than 17% of the total corrections made via data assimilation system.

[53] These results have practical implication to coastal studies of biochemical tracer transport. The importance of remote forcing and large-scale energy propagation into the local coastal region are evidence that observing systems should be required to account for the larger-scale circulation to understand the modulation of the coastal flow.

[54] **Acknowledgments.** Janeković was supported on NOAA grant NA10NOS4730016, Powell was supported by the Office of Naval Research grant N00014-09-10939, Matthews was supported by NOAA grant NA07NOS4730207, and McManus was supported on NOAA grant NA10NOS4730016. We are grateful to the comments by the reviewers which led to substantial improvements in the manuscript. All the figures were made using the NCAR Command Language Software (NCL) <http://dx.doi.org/10.5065/D6WD3XH5>.

## References

- Alford, M. H., M. C. Gregg, and M. A. Merrifield (2006), Structure, propagation, and mixing of energetic baroclinic tides in Mamala Bay, Oahu, Hawaii, *J. Phys. Oceanogr.*, *36*, 997–1018.
- Barron, C. N., C. A. Kara, P. J. Martin, R. C. Rhodes, and L. F. Smedstad (2006), Formulation, implementation and examination of vertical coordinate choices in the global Navy Coastal Ocean Model (NCOM), *Ocean Modell.*, *11*, 347–375.
- Broquet, G., C. A. Edwards, A. Moore, B. S. Powell, M. Veneziani, and J. D. Doyle (2009), Application of 4D-Variational data assimilation to the California Current System, *Dyn. Atmos. Oceans*, *48*, 69–92.
- Broquet, G., A. M. Moore, H. G. Arango, and C. A. Edwards (2011), Corrections to ocean surface forcing in the California Current System using 4D variational data assimilation, *Ocean Modell.*, *36*, 116–132.
- Carter, G. S., M. A. Merrifield, J. Becker, K. Katsumata, M. C. Gregg, D. S. Luther, M. D. Levine, T. J. Boyd, and Y. L. Firing (2008), Energetics of  $M_2$  barotropic-baroclinic tidal conversion at the Hawaiian Islands, *J. Phys. Oceanogr.*, *38*, 2205–2223.
- Chapman, D. C. (1985), Numerical treatment of cross-shelf open boundaries in a barotropic coastal ocean model, *J. Phys. Oceanogr.*, *15*, 1060–1075.
- Chavanne, C., P. Flament, R. Lumpkin, B. Dousset, and A. Bentamy (2002), Scatterometer observations of wind variations induced by oceanic islands: Implications for wind-driven ocean circulation, *Can. J. Remote Sens.*, *28*, 466–474.
- Chavanne, C., P. Flament, G. Carter, M. A. Merrifield, and D. S. Luther (2010), The surface expression of semidiurnal internal tides near a strong source at Hawaii. Part I: Observations and numerical predictions, *J. Phys. Oceanogr.*, *40*, 1155–1179.
- Courtier, P., J. N. Thépaut, and A. Hollingsworth (1994), A strategy for operational implementation of 4D-Var, using an incremental approach, *Q. J. R. Meteorol. Soc.*, *120*, 1367–1387.
- Demirov, E., N. Pinardi, C. Fratianni, M. Tonani, L. Giacomelli, and P. D. Mey (2003), Assimilation scheme of the Mediterranean Forecasting System: Operational implementation, *Ann. Geophys.*, *21*, 189–204.
- Dong, C., and J. C. McWilliams (2007), A numerical study of island wakes in the Southern California Bight, *Cont. Shelf Res.*, *27*, 1233–1248.

- Egbert, G. D., and S. Y. Erofeeva (2002), Efficient inverse modeling of barotropic ocean tides, *J. Atmos. Oceanic Technol.*, *19*, 183–204.
- Fairall, C. W., E. F. Bradley, D. P. Rogers, J. B. Edson, and G. S. Young (1996), Bulk parameterization of air-sea fluxes for tropical ocean-global atmosphere Coupled-Ocean Atmosphere Response Experiment, *J. Geophys. Res.*, *101*, 3747–3764.
- Fennel, K., J. Wilkin, J. Levin, J. Moisan, J. O'Reilly, and D. Haidvogel (2006), Nitrogen cycling in the Middle Atlantic Bight: Results from a three-dimensional model and implications for the North Atlantic nitrogen budget, *Global Biogeochem. Cycles*, *20*, GB3007, doi:10.1029/2005GB002456.
- Fiechter, J., A. M. Moore, C. A. Edwards, K. W. Bruland, E. D. Lorenzo, C. V. W. Lewis, T. M. Powell, E. N. Curchitser, and K. Hedstrom (2009), A simple approach to model iron limitation on primary production in the coastal Gulf of Alaska, *Deep Sea Res., Part II*, *56*, 2503–2519, doi:10.1016/j.dsr2.2009.02.010.
- Hoteit, I., B. Cornuelle, A. Köhl, and D. Stammer (2005), Treating strong adjoint sensitivities in tropical eddy-permitting variational data assimilation, *Q. J. R. Meteorol. Soc.*, *131*, 3659–3682.
- Janeković, I., and B. S. Powell (2012), Analysis of imposing tidal dynamics to nested numerical models, *Cont. Shelf Res.*, *34*, 30–40, doi:10.1016/j.csr.2011.11.017.
- Karl, D. M., and R. Lukas (1996), The Hawaii Ocean Time-Series (HOT) program: Background, rationale and field implementation, *Deep Sea Res., Part II*, *43*, 129–156.
- Köhl, A., and J. Willebrand (2002), An adjoint method for the assimilation of statistical characteristics into eddy-resolving ocean models, *Tellus A*, *54*, 406–425.
- Köhl, A., D. Stammer, and B. Cornuelle (2007), Interannual to decadal changes in the ECOO global synthesis, *J. Phys. Oceanogr.*, *37*, 313–337.
- Lumpkin, R. (1998), Eddies and currents of the Hawaiian Islands, PhD thesis, 282 pp., SOEST-School of Ocean and Earth Sci. and Technol., Univ. of Hawaii at Manoa.
- Lumpkin, R., and P. J. Flament (2013), Extent and energetics of the Hawaiian lee countercurrent, *Oceanography*, *26*, 58–65.
- Marchesiello, P., J. C. McWilliams, and A. F. Shchepetkin (2001), Open boundary conditions for long term integration of regional oceanic models, *Ocean Modell.*, *3*, 1–20.
- Matthews, D., B. S. Powell, and I. Janeković (2012), Analysis of four-dimensional variational state estimation of the Hawaiian waters, *J. Geophys. Res.*, *117*, C03013, doi:10.1029/2011JC007575.
- McManus, M. A., K. J. Benoit-Bird, and C. B. Woodson (2008), Behavior exceeds physical forcing in the diel horizontal migration of the midwater sound-scattering layer in Hawaiian waters, *Mar. Ecol. Prog. Ser.*, *365*, 91–101.
- Mellor, G. L., and T. Yamada (1982), Development of a turbulence closure model for geophysical fluid problems, *Rev. Geophys. Space Phys.*, *20*, 851–875.
- Merrifield, M. A., and P. E. Holloway (2002), Model estimates of M2 internal tide energetics at the Hawaiian Ridge, *J. Geophys. Res.*, *107*(C8), 3179, doi:10.1029/2001JC000996.
- Moore, A. M., H. G. Arango, E. D. Lorenzo, B. D. Cornuelle, A. J. Miller, and D. J. Neilson (2004), A comprehensive ocean prediction and analysis system based on the tangent linear and adjoint of a regional ocean model, *Ocean Modell.*, *7*, 227–258.
- Moore, A. M., H. G. Arango, G. Broquet, C. Edwards, M. Veneziani, B. S. Powell, D. Foley, J. Doyle, D. Costa, and P. Robinson (2011a), The Regional Ocean Modeling System (ROMS) 4-dimensional variational data assimilation systems. II: Performance and application to the California current system, *Prog. Oceanogr.*, doi:10.1016/j.pocean.2011.05.003.
- Moore, A. M., H. G. Arango, G. Broquet, B. S. Powell, J. Zavala-Garay, and A. T. Weaver (2011b), The Regional Ocean Modeling System (ROMS) 4-dimensional variational data assimilation systems, *Prog. Oceanogr.*, doi:10.1016/j.pocean.2011.05.004.
- Nash, J. D., E. Kunze, C. M. Lee, and T. B. Sanford (2006), Structure of the baroclinic tide generated at Kaena Ridge, Hawaii, *J. Phys. Oceanogr.*, *36*, 1123–1135.
- Nguyen, H. V., Y. L. Chen, and F. Fujioka (2010), Numerical simulations of island effects on airflow and weather during the summer over the Island of Oahu, *Mon. Weather Rev.*, *128*, 2253–2280.
- Powell, B. S., H. G. Arango, A. M. Moore, E. Di Lorenzo, R. F. Milliff, and D. Foley (2008), 4DVAR data assimilation in the Intra-Americas Sea with the Regional Ocean Modeling System (ROMS), *Ocean Modell.*, *25*, 173–188.
- Powell, B. S., A. M. Moore, H. G. Arango, R. F. Milliff, and R. R. Leben (2009), Real-time assimilation and prediction in the Intra-Americas Sea with the Regional Ocean Modeling System (ROMS), *Dyn. Atmos. Oceans*, *48*, 46–68.
- Powell, B. S., I. Janeković, G. S. Carter, and M. A. Merrifield (2012), Sensitivity of internal tide generation in Hawaii, *Geophys. Res. Lett.*, *39*, L10606, doi:10.1029/2012GL051724.
- Shchepetkin, A. F., and J. C. McWilliams (2003), A method for computing horizontal pressure-gradient force in an oceanic model with nonaligned vertical coordinate, *J. Geophys. Res.*, *108*(C3), 3090, doi:10.1029/2001JC001047.
- Shchepetkin, A. F., and J. C. McWilliams (2005), The Regional Oceanic Modeling System: A split-explicit, free-surface, topography-following-coordinate ocean model, *Ocean Modell.*, *9*, 347–404.
- Sikirić, M. D., I. Janeković, and M. Kuzmić (2009), A new approach to bathymetry smoothing in sigma-coordinate ocean models, *Ocean Modell.*, *29*, 128–136, doi:10.1016/j.ocemod.2009.03.009.
- Stammer, D., C. Wunsch, R. Giering, C. Eckert, P. Heimbach, J. Marotzke, A. Adcroft, C. N. Hill, and J. Marshall (2002), The global ocean circulation during 1992–1997, estimated from ocean observations and a general circulation model, *J. Geophys. Res.*, *107*(C9), 3118, doi:10.1029/2001JC000888.
- Stammer, D., C. Wunsch, R. Giering, C. Eckert, P. Heimbach, J. Marotzke, A. Adcroft, C. N. Hill, and J. Marshall (2003), Volume, heat and freshwater transports of the global ocean circulation 1993–2000, estimated from a general circulation model constrained by WOCE Data, *J. Geophys. Res.*, *108*(C1), 3007, doi:10.1029/2001JC001115.
- Stammer, D., K. Ueyoshi, A. Köhl, W. B. Large, S. Josey, and C. Wunsch (2004), Estimating air-sea flux estimates through global ocean data assimilation, *J. Geophys. Res.*, *109*, C05023, doi:10.1029/2003JC002082.
- Weaver, A., and P. Courtier (2001), Correlation modelling on the sphere using generalized diffusion equation, *Q. J. R. Meteorol. Soc.*, *127*, 1815–1846.
- Wolanski, E., T. Asaeda, A. Tanaka, and E. Deleersnijder (1996), Three-dimensional island wakes in the field, laboratory experiments and numerical models, *Cont. Shelf Res.*, *16*, 1437–1452.
- Xie, S.-P., W. Liu, Q. Liu, and M. Nonaka (2001), Far-reaching effects of the Hawaiian Islands on the Pacific ocean-atmosphere system, *Science*, *292*(5524), 2057–2060.
- Zhu, J., M. Kamachi, and W. Hui (2002), The improvement made by a modified TLM in 4D-Var with a geophysical boundary layer model, *Adv. Atmos. Sci.*, *19*, 563–582.